The Astrophysical Journal, 801:53 (14pp), 2015 March 1 doi:10.1088/0004-637X/801/1/53
© 2015. The American Astronomical Society. All rights reserved.

# ON THE NEED FOR THE LIGHT ELEMENTS PRIMARY PROCESS (LEPP)

S. Cristallo[1,2], C. Abia[3], O. Straniero[1,2], and L. Piersanti[1,2]
[1] INAF-Osservatorio Astronomico di Collurania, I-64100 Teramo, Italy
[2] INFN Sezione Napoli, Napoli, Italy
[3] Departamento de Física Teórica y del Cosmos, Universidad de Granada, E-18071 Granada, Spain
*Received 2014 October 8; accepted 2015 January 1; published 2015 March 4*

## ABSTRACT

Extant chemical evolution models underestimate the galactic production of Sr, Y, and Zr as well as the solar system abundances of s-only isotopes with $90 < A < 130$. To solve this problem, an additional (unknown) process has been invoked, the so-called light element primary process (LEPP). In this paper we investigate possible alternative solutions. Based on Full Network Stellar evolutionary calculations, we investigate the effects on the solar system s-only distribution induced by the inclusion of some commonly ignored physical processes (e.g., rotation) or by the variation of the treatment of convective overshoot, mass loss, and the efficiency of nuclear processes. Our main findings are (1) at the epoch of the formation of the solar system, our reference model produces supersolar abundances for the whole s-only distribution, even in the range $90 < A < 130$, (2) within errors, the s-only distribution relative to $^{150}$Sm is flat, (3) the s-process contribution of the less massive AGB stars ($M < 1.5\,M_{\odot}$) as well as of the more massive ones ($M > 4.0\,M_{\odot}$) are negligible, (4) the inclusion of rotation implies a downward shift of the whole distribution with a higher efficiency for the heavy s-only isotopes, leading to a flatter s-only distribution, (5) different prescriptions on convection or mass loss produce nearly rigid shifts of the whole distribution. In summary, a variation of the standard paradigm of AGB nucleosynthesis would allow reconciliation of model predictions with solar system s-only abundances. Nonetheless, the LEPP cannot be definitely ruled out because of the uncertainties still affecting stellar and galactic chemical evolution models.

*Key words:* nuclear reactions, nucleosynthesis, abundances – stars: AGB and post-AGB

## 1. INTRODUCTION

Mass-losing asymptotic giant branch (AGB) stars are the main source of medium- and long-term gas returned to the interstellar medium (ISM). For this reason, they allow late episodes of stellar formation, thus prolonging the star-forming lifetime in many different galactic environments. In addition, as a result of a complex combination of internal nucleosynthesis and deep convective mixing, the wind of AGB stars is heavily enriched in both light (C, N, F, Na) and heavy elements. About half of the isotopes from Sr to Pb are produced by AGB stars in their interior through a slow neutron capture process called the s process (see, e.g., Busso et al. 1999). Moreover, the dust forming in their cool extended circumstellar envelopes efficiently pollutes the ISM. Therefore, AGB stars play a fundamental role in the chemical evolution of galaxies.

In this paper we discuss the evolution of the heavy elements $A > 90$ in the solar neighborhood. Our main goal is to understand if the current nucleosynthesis models provide a reliable evaluation of the ISM contamination by AGB stars. The main and the strong components of the s process $A > 90$ are produced by low-mass AGB stars, typically $1.5 < M/M_{\odot} \leqslant 3.0$. Lighter s elements $A < 90$ are mainly synthesized by the s process in massive stars during core He burning and shell C burning (the so-called weak component; Kappeler et al. 1989; Beer et al. 1992; Pignatari et al. 2010). Massive stars are also responsible for the r process (rapid neutron capture nucleosynthesis; for a review see Sneden et al. 2008). Most of the isotopes heavier than iron are produced by both the s and r processes. However, there exist a few isotopes that cannot receive any contribution from the r process and, for this reason, are called s-only isotopes. An s-only isotope with atomic number $Z$ is shielded by the r process because of the existence of a stable isobar with $Z$-1 or $Z$-2. For this reason, the sequence of $\beta$ decays that occurs at the end of the r process is interrupted before the s-only nucleus is reached.

Galactic chemical evolution (GCE) models obtained by combining the s process contribution of AGB stars (main and strong components) and massive stars (weak s and r processes) have been studied by Travaglio et al. (1999, 2001, 2004) and Bisterzo et al. (2014). Travaglio et al. (2004) first reported a deficit of the predicted solar system abundances of Sr, Y, and Zr (about −18%). These three elements belong to the first s-process peak in the solar system composition, which corresponds to nuclei with the magic neutron number $N = 50$. After analyzing the possible uncertainties in their nucleosynthesis calculations, they concluded that this deficit would imply the existence of a missing s-process contribution, the so-called light element primary process (LEPP). Note that a different LEPP has also been invoked to explain the abundances of a large group of light elements with an important contribution from the r process. For instance, Montes et al. (2007) distinguished between "solar" and "stellar" LEPP, the latter being linked to r-enhanced low-metallicity halo stars. Our findings are limited to the main s process from AGB stars, so we only focus on s-only isotopes in the solar nebula. Therefore, the results presented in this paper do not provide any hint to certify (or exclude) the existence of a metal-poor primary LEPP, which could equally well have its roots in a sort of weak r process.

The need for an unknown pure s-process contribution has also been claimed by Bisterzo et al. (2014) based on the analysis of the s-only isotopes (see also Käppeler et al. 2011). Indeed, in their chemical evolution models, all of the s-only isotopes with $90 < A < 130$ are systematically underestimated. As a matter of fact, the AGB yields used by Travaglio et al. (2004) and Bisterzo et al. (2014) are based on postprocess

calculations (Gallino et al. 1998) in which the main neutron source (the $^{13}$C pocket) is artificially introduced. The s process in low-mass AGB stars is mainly due to the neutrons released by the $^{13}$C($\alpha$,n)$^{16}$O reaction in a thin $^{13}$C pocket that forms after each third dredge-up (TDU) episode (Straniero et al. 1995; Gallino et al. 1998; Straniero et al. 2006). At present, a reliable evaluation of the extension in mass and of the $^{13}$C profile within the pocket is probably the most challenging task for AGB stellar modelers (Herwig et al. 1997; Denissenkov & Tout 2003; Cristallo et al. 2009, 2011; Liu et al. 2014). In the GCE models by Bisterzo et al. (2014), the extension of the $^{13}$C pocket as well as the mass fractions of $^{13}$C and $^{14}$N (the main neutron source and the main neutron poison, respectively) are freely varied in order to reproduce the 100% solar $^{150}$Sm with an s-only distribution as flat as possible. These authors, however, did not explore the physical motivation at the base of those variations. More recently, Trippella et al. (2014) argued that, in stars with $M < 1.5\,M_{\odot}$, magnetic fields are able to shape larger $^{13}$C pockets than those characterizing more massive AGBs (see also Maiorca et al. 2012), and they suggest that this occurrence might have important consequences for the solar system s-only distribution. However, their conclusions have to be verified with the support of a GCE model as well as evolutionary models that include the feedback of magnetic fields.

The analysis of the LEPP problem presented in this work is based on a different approach. We verify if our Full Network Stellar (FUNS; see Straniero et al. 2006 and references therein) yields, incorporated into a chemical evolution model for the solar neighborhood, can provide a reasonable fit to the solar system s-only distribution. The adoption of a large nuclear network directly coupled to the physical evolution of the stars and our handling of the convective/radiative interface at the base of the convective envelope (i.e., where the $^{13}$C forms) do not allow us to force our calculation to fit the absolute value of the solar system s-only distribution. Nevertheless, we can evaluate the effects on the AGB nucleosynthesis of different prescriptions for convective overshoot during the TDU, rotation-induced mixing, pre-AGB, and AGB mass-loss rates and nuclear reaction efficiencies.

The paper is structured as follows. We first describe our galactic chemical evolution model and the stellar evolutionary code used to determine the protosolar distribution for s-only isotopes. (Section 2 and Section 3, respectively). Then, in Section 4 we present our reference case, and in Sections 5 and 6 we describe how AGB model uncertainties affect our results. Our conclusions follow in Section 7.

## 2. THE GALACTIC CHEMICAL EVOLUTION MODEL

We use a simplified GCE model for the solar neighborhood, defined as a cylinder of ~1 kpc radius at a distance of ~8 kpc from the Galactic center, adopting the standard formalism (e.g., Pagel 2009). Our GCE code is an update of that used to follow the evolution of light elements in previous studies (Abia et al. 1991, 1995). The classical set of equations are solved numerically without the instantaneous recycling approximation (i.e., stellar lifetimes are taken into account) and assuming that at the star's death its ejecta are thoroughly mixed instantaneously in the local ISM, which is then characterized by a unique composition at a given time. Thus, our predictions represent average values in time because this simplified approach cannot account for the scatter in any galactic observable. Our main goal is to reproduce the absolute and relative isotopic abundance distributions of s-only nuclei at the solar system formation (which occurred 4.56 Gyr ago). These nuclei are $^{70}$Ge, $^{76}$Se, $^{80,82}$Kr, $^{86,87}$Sr, $^{96}$Mo, $^{100}$Ru, $^{104}$Pd, $^{110}$Cd, $^{116}$Sn, $^{122,123,124}$Te, $^{128,130}$Xe, $^{134,136}$Ba, $^{142}$Nd, $^{148,150}$Sm, $^{154}$Gd, $^{160}$Dy, $^{170}$Yb, $^{176}$Lu, $^{176}$Hf, $^{186}$Os, $^{192}$Pt, $^{198}$Hg, and $^{204}$Pb. We concentrate on those isotopes because they are produced only via the s process and because an AGB origin is certain for those with atomic mass $A \geqslant 96$. We use the absolute isotopic abundances of the protosolar nebula to normalize the output of our GCE model, which is stopped at that epoch. Note that those abundances differ from the current ones observed in the solar photosphere due to the impact of chemical settling. We obtain our protosolar distribution by adopting the elemental abundances of Lodders et al. (2009) and by computing a Standard Solar Model according to the procedure described in Piersanti et al. (2007).

The basic ingredients of the GCE model are described in the following. For the stellar yields see Section 3.

We adopt a standard Salpeter initial mass function (IMF), $\Phi(M) \propto M^{-(1+X)}$, with $X = 1.35$ in the mass range 0.1–100 $M_{\odot}$. For the star-formation rate (SFR) we have adopted the standard Schmidt-type law $\Psi(t) = \alpha\sigma_{\rm gas}^{k}(t)$, where $\sigma_{\rm gas}$ is the surface gas density, $\alpha = 0.32\,{\rm Gyr}^{-1}$, and $k = 1$. We assume that the disk has been built up starting from an initial surface gas density ($\sigma_o$) and by slow accretion of gas with primordial composition. Hence the initial abundances of all of the studied isotopes are set to zero. We adopt an exponentially decreasing gas accretion law $f(t) \propto e^{-t/\tau}$. This infall prescription, combined with the adopted SFR law, leads to a decreasing star-formation history in the solar neighborhood. We set $\tau = 7.5$ Gyr because it has been shown that such a long timescale provides a satisfactory fit to the observed stellar metallicity distribution (MD) in the solar neighborhood (e.g., Boissier & Prantzos 1999). We have normalized the infall rate $f(t)$ by imposing that the current observed total surface density is $\sim 50\,M_{\odot}\,{\rm pc}^{-2}$ (see Goswami & Prantzos 2000 and references therein for a detailed discussion).

The main observables in the solar neighborhood that must be fitted are

1. the current surface density of gas ($13 \pm 3\,M_{\odot}$ pc$^{-2}$; gas fraction 0.15–0.25%), stellar surface density ($35 \pm 5\,M_{\odot}$ pc$^{-2}$), total mass ($\sim 50\,M_{\odot}$ pc$^{-2}$), and the current SFR (2–5 $M_{\odot}$ Gyr$^{-1}$pc$^{-2}$) (Boissier & Prantzos 1999; Goswami & Prantzos 2000);
2. the observed age–metallicity relation (e.g., Casagrande et al. 2011);
3. the type II and Ia supernova rates in the Galaxy (Li et al. 2011), and the observed [O/Fe] versus [Fe/H] relationship in thin and thick disk stars (e.g., Ramírez 2013; Nissen et al. 2014);
4. the observed MD of long-lived G-type stars (Casagrande et al. 2011; Adibekyan et al. 2012; Bensby et al. 2014);
5. the absolute and relative s-only isotopic abundance distribution at the formation of the solar system (Lodders et al. 2009).

Recent studies (Roskar et al. 2008; Schönrich and Binney 2009; Kubryk et al. 2013) have shown that the existence of gas and star migration across the disk of the Milky Way can significantly alter the local observed age–metallicity relation and the stellar MD. One of the main conclusions of

those studies is that these observational constraints can be properly interpreted only if the migration of stars and gas is included in GCE models. For instance, recent GCE models that include migration show that the average age–metallicity relation for stars locally born is generally flatter than the one calculated classically (i.e., without migration, as is typically done in one-zone, 1D GCE models). In particular, this implies that the Sun was probably not born locally but migrated from inner (more metal-rich) Galactic regions up to its current position ($r \sim 8$ kpc). Stellar migration also introduces a dispersion in the observed abundance ratios as a function of the metallicity (i.e., [X/Fe] versus [Fe/H]). Although this dispersion seems to be generally small ($\sigma < 0.15$ dex), it might be larger for elements produced in low-mass, long-lived stars, like Fe or s elements. Furthermore, the average gas metallicity in the ISM might differ from that of the local stellar population. The impact of the gas and star migration in the observed s-element distribution in the solar system is beyond the scope of this study. We refer to specific studies (Kubryk et al. 2013) for a detailed discussion on the effects of migration on the chemical evolution of the Galaxy.

Note that we cannot a priori exclude that the simplifications inherent in our GCE code mask some chemical features or introduce some biases in following the chemical evolution of s-only isotopes. Indeed, we are aware that more sophisticated models than the one-zone GCE approximation adopted in the present work can be constructed for the solar neighborhood. We refer, for instance, to works including the evolution of the halo and of the thick disk (Goswami & Prantzos 2000; Kobayashi et al. 2000; Micali et al. 2013). Different prescriptions for the SFR and infall/outflow of gas are typically adopted for the evolution of these two galactic structures, which are mainly constrained by their observed MD function. Nonetheless, we have checked that our results for the s-only isotope abundance distribution are not affected when adding, for instance, the halo evolution (according to the Goswami & Prantzos 2000 prescriptions), provided that the initial metallicity for the disk evolution does not significantly exceed [Fe/H]$\sim -1.0$. Typically, this is the maximum value of the metallicity for the halo reached in most GCE models after $t \sim 1$ Gyr.

## 3. STELLAR MODELS

Stellar lifetimes, remnant masses, and yields for low- and intermediate-mass stars (IMS) ($1.0 \leqslant M/M_{\odot} \leqslant 6.0$) are derived from theoretical evolutionary models computed with the FUNS evolutionary code (Straniero et al. 2006).[4] The stellar yields have been obtained by evolving models with different masses and initial chemical composition from the pre–main sequence up to the AGB tip. In our models, the adopted AGB mass-loss rate has been calibrated on the period–luminosity and period–mass loss relations observed in long-period variable stars (see Straniero et al. 2006 and references therein). The atomic and molecular opacities in the cool envelope of AGBs account for the variation of the chemical composition as being due to the occurrence of recurrent TDU episodes (Cristallo et al. 2007). During TDU episodes, the instability occurring at the inner border of the convective envelope is handled by adopting an exponential decay of the convective velocities. This makes the TDU deeper; moreover, as a byproduct, we obtain the self-consistent formation of the $^{13}$C pocket after each thermal pulse (TP) followed by TDU (Cristallo et al. 2009; Straniero et al. 2014). The extension of the $^{13}$C pocket varies from TP to TP following the shrinking of the region between the He and the H shells (the so-called He intershell). The nuclear network used to follow the physical and chemical evolution of our models has been presented in Cristallo et al. (2011): it includes about 500 isotopes (from hydrogen to bismuth) linked by more than 1,000 reactions. Such a network is directly included in the FUNS code, thus avoiding the use of postprocess techniques.

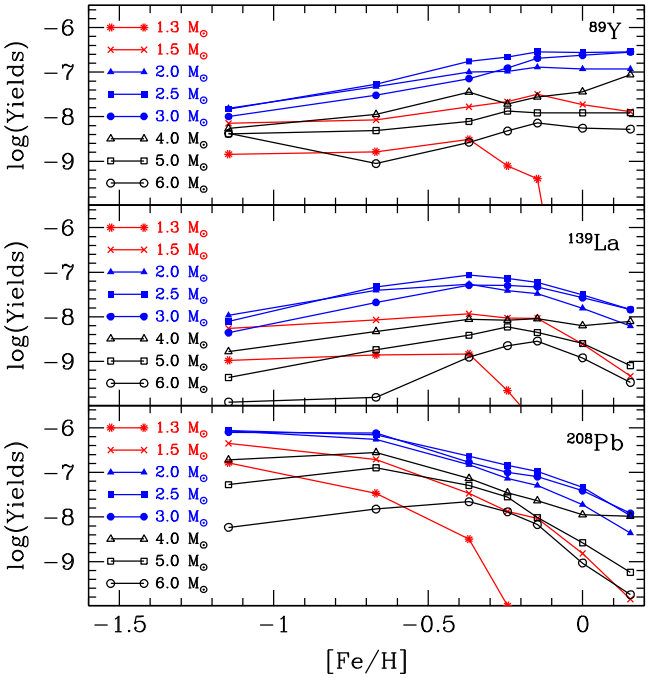



**Figure 1.** Selection of FRUITY yields for key s-process elements. Upper panel: $^{89}$Y (representative of the first s-process peak), intermediate panel: $^{139}$La (representative of the second s-process peak), lower panel: $^{208}$Pb (representative of the third s-process peak).

The main neutron source in AGB stars is represented by the $^{13}$C($\alpha$,n)$^{16}$O reaction, burning in radiative conditions at $T \sim 10^8$ K during the interpulse phases. An additional contribution comes from the activation of the $^{22}$Ne($\alpha$,n)$^{25}$Mg reaction at the base of the convective shells generated by TPs when the temperature exceeds $3 \times 10^8$ K. Whereas the former reaction dominates the s-process nucleosynthesis in low-mass AGB stars, the latter becomes fully efficient in stars with $M \geqslant 3\,M_{\odot}$.[5] The models we use to calculate the AGB yields have different masses ($1.0 \leqslant M/M_{\odot} \leqslant 6.0$) and metallicities ($-2.15 <$ [Fe/H] $< +0.15$; Cristallo et al. 2009, 2011; S. Cristallo et al. 2015, in preparation). The corresponding yields are available online on our Web repository FRUITY,[6] which represents our reference set.

In Figure 1 we report a selection of FRUITY net yields[7] for some key s-process elements ($^{89}$Y as representative of the

[4] The FUNS code has been derived from the FRANEC code (Chieffi & Straniero 1989; Chieffi et al. 1998).

[5] This mass limit depends on the metallicity. As a general rule, the minimum mass decreases with the metallicity.

[6] http://fruity.oa-teramo.inaf.it

[7] A net yield is defined as

$$\int_0^{\tau(M_i)} \left[X(k) - X^0(k)\right] \frac{dM}{dt} dt \qquad (1)$$

where $dM/dt$ is the mass loss rate, while $X(k)$ and $X^0(k)$ stand for the current and the initial mass fraction of the $k$ isotope, respectively.

first s-process peak, $^{139}$La as representative of the second s-process peak, and $^{208}$Pb as representative of the third s-process peak). As already remarked in Cristallo et al. (2011), the largest yields are produced in the (1.5–3.0) $M_{\odot}$ mass range. Figure 1 shows that low-mass models ($M < 1.5\,M_{\odot}$) marginally contribute to the global s-process production because the TDU practically ceases to occur when the initial stellar mass drops below $1.2\,M_{\odot}$ (see also Section 5.3). Similarly, s-process yields from more massive AGBs ($M > 4.0\,M_{\odot}$) are low, even if these stars may significantly contribute to the nucleosynthesis of some neutron-rich isotopes (for example, $^{87}$Rb and $^{96}$Zr) due to the activation of the $^{22}$Ne($\alpha$,n)$^{25}$Mg reaction. As expected, for stars with masses between 1.5 and $3.0\,M_{\odot}$, the relative distribution of the three s-process peaks weakly depends on the mass, whereas it has a different behavior depending on the initial iron content. At large metallicities ([Fe/H] $> -0.3$), the s process mainly populates the first peak (Sr–Y–Zr region). At intermediate metallicities, the second s-process peak (Ba–La–Ce–Nd region) presents its maximum. At low metallicities ([Fe/H] $\lesssim -0.7$), lead production dominates.

In our GCE, we adopt a simplified prescription by assuming that all stars with mass $M > 8\,M_{\odot}$ explode as core collapse supernovae, leaving behind a compact remnant such as a neutron star of mass $\lesssim 1.4\,M_{\odot}$ or a black hole in the case of most massive stars ($M > 40\ M_{\odot}$). In our calculations, we do not include the contribution of massive stars to the s-process inventory. Those stars largely contribute to the production of s-only isotopes with $A < 87$ (see Pignatari et al. 2010 and references therein). Therefore, for those isotopes our predictions have to be considered as lower limits. Oxygen and iron yields from massive stars are instead needed in order to reproduce the average [O/Fe] versus [Fe/H] relationship observed in unevolved stars (e.g., Ramírez 2013; Nissen et al. 2014). For that purpose, we use the yields published by Chieffi & Limongi (2004). As far as it concerns the core-collapse supernovae contribution to the iron enrichment, we assume that on average each supernova ejects $0.1\,M_{\odot}$ of $^{56}$Fe. On the other hand, we adopt the type Ia supernovae explosion rate according to Greggio & Renzini (1983) in the framework of the single degenerate scenario for their progenitors. This corresponds to assuming that a fraction of 2.5% of all binary systems ever formed in the adequate mass range will provide an explosive outcome. This fraction value is set by fitting the observed current galactic SN Ia rate and the [O/Fe] versus [Fe/H] relationship. We also assume that, on average, for each SN Ia event, an amount of $\sim 0.7\,M_{\odot}$ of $^{56}$Fe is ejected (e.g., Bravo & Martínez-Pinedo 2012).

## 4. REFERENCE CASE

Our *Reference* case has been computed using the GCE model described in Section 2 by adopting the parameter values reported there. The model accounts for all of the constraints mentioned above within the observational uncertainties. It is very well known that other reasonable choices for the GCE model parameters (SFR law, IMF, etc.) might give similar results still in good agreement with the observational constraints. Because of its relevance for our discussion, we show in Figure 2 the age–metallicity relation obtained in the *Reference* case (thick continuous line). The dotted curves represent the average and $\pm 1\sigma$ limits of the observations of Casagrande et al. (2011) and Bensby et al. (2014). Our model predicts a rapid increase of the ISM metallicity with time, reaching [Fe/H] $\approx 0.0$ at the epoch of solar system formation and a continuous increase of [Fe/H] until now.

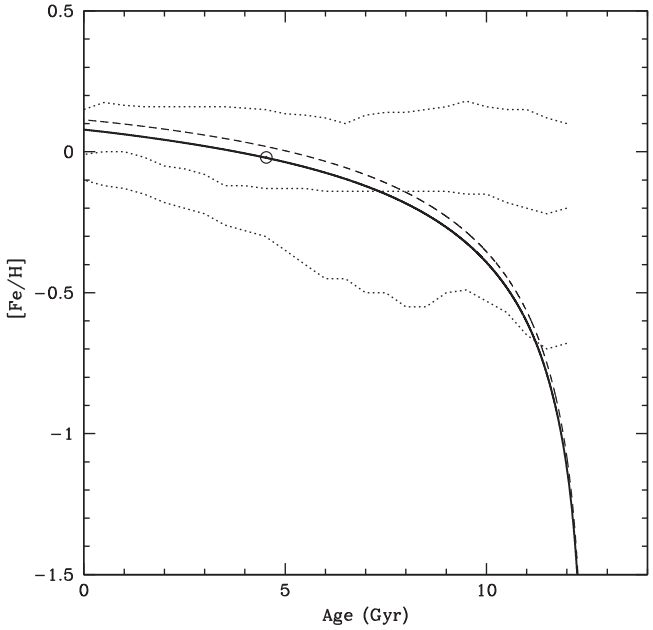



**Figure 2.** Age–metallicity relation (solid thick curve) compared to the average and $\pm 1\sigma$ limits (dotted curves) of the observations in the solar neighborhood by Casagrande et al. (2011) and Bensby et al. (2014). The dashed curve refers to a GCE model computed with an increased SFR (+10% with respect to the solid thick curve). See Section 6 for details.

In Figure 3 we report the results of our *Reference* GCE calculation case, as obtained by using stellar yields included in the FRUITY database. The corresponding data are reported in Table 1. In the upper panel we report absolute percentage s-only isotopic abundances obtained from our GCE model at the epoch of the solar system formation. In this plot we did not add any contribution from the weak s process. Thus, 100% means that an isotope is entirely synthesized by AGB stars. For each isotope, we also plot the corresponding solar abundance uncertainty reported in Lodders et al. (2009). Dashed horizontal lines identify a $\pm 10\%$ tolerance region representing the current uncertainties in the estimated chemical abundances as due to nuclear cross sections (Käppeler et al. 2011). In the lower panel of Figure 3, we report the overproduction factors normalized with respect to $^{150}$Sm. In this case, unity means that an s-only isotope is overproduced (or underproduced) as $^{150}$Sm with respect to the corresponding solar abundance. The latter isotope has been chosen as reference because the entire s-process flux passes through it, making this isotope virtually unbranched (Arlandini et al. 1999). Also in this case, we highlight a $\pm 10\%$ tolerance region.

An inspection of Figure 3 (upper panel) reveals an overall overproduction of s-only isotopes with $A \geqslant 96$ ($\sim 145\%$), more evident in the region $128 \leqslant A \leqslant 204$. Thus, on a relative scale, lighter s-only isotopes are underproduced with respect to the heaviest ones (see lower panel of Figure 3). However, our relative distribution can be considered flat if current uncertainties (observational and nuclear) are taken into

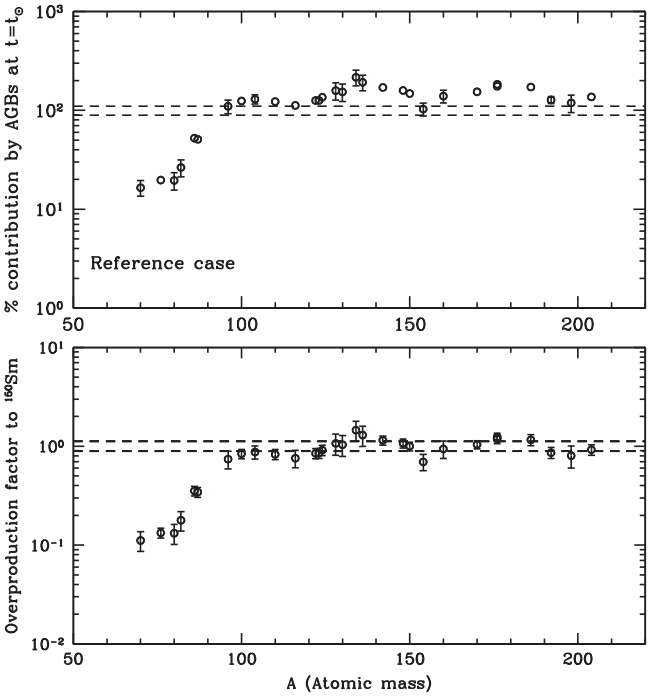



**Figure 3.** Reference GCE calculation case. Upper panel: percentage s-only isotopic abundances at the epoch of the solar system formation. Solar abundance errors are taken from Lodders et al. (2009) and reported in Table 1 (error bars smaller than symbols are not reported). Lower panel: overproduction factors normalized to the $^{150}$Sm one. Dashed horizontal lines identify a ±10% tolerance region in both panels. See text for details.

account. Because we do not assume any ad hoc rescaling of the $^{13}$C pocket, at odds with Travaglio et al. (2004) and Bisterzo et al. (2014), who claimed a missing contribution to light s-only isotopes, we obtain supersolar percentages for all s-only isotopes with a sure AGB origin ($A \geqslant 96$). Thus, in the following we investigate if there is the possibility to decrease the overall galactic s-only production and if a larger depletion efficiency can be found for the heavier s-only isotopes ($128 \leqslant A \leqslant 204$). This exploration is carried out in the next section by studying current uncertainties affecting stellar models.

As a starting point for our analysis, however, we want to verify if GCE models confirm that the bulk of the s process comes from AGB stars with masses $1.5 \leqslant M/M_{\odot} \leqslant 3.0$ (see previous section). The contribution from AGBs with $M < 1.5\,M_{\odot}$ will be analyzed in Section 5.3. In order to quantify the contribution to the solar system s-only distribution from IMS AGBs, we run a GCE model by setting to zero the yields of stars with initial mass $M > 4\,M_{\odot}$ (hereinafter the No IMS case). The results are shown in Figure 4 and reported in Table 1. On average, the IMS contribution to the solar system s-only distribution is marginal (on average 6%). Thus, even if our IMS AGBs present a tiny $^{13}$C pocket after TDUs (Straniero et al. 2014), their contribution, once weighted on the IMF, is small. For the lightest s-only isotopes (from $^{70}$Ge to $^{87}$Sr), the relative IMS contribution is larger because of the more efficient activation of the $^{22}$Ne($\alpha$,n)$^{25}$Mg source. Note, however, that those isotopes are mainly synthesized by the weak s component (Kaeppeler et al. 1994; Pignatari et al. 2010). Thus, we basically confirm the finding of Bisterzo et al. (2014) that intermediate-mass AGBs marginally contribute to the galactic chemical evolution of s-only isotopes.

## 5. STELLAR MODEL UNCERTAINTIES

Despite great strides made by stellar modelers in the last two decades, our understanding of the AGB phase is still hampered by large uncertainties. A few physical details can be constrained by theory, so the adoption of phenomenological models is often the only way to describe a specific physical process. Thus, it is not surprising that a large part of the extant models still include a set of parameters that are sometimes rather free, sometimes (partially) constrained by observations. Despite all of these limitations, we try to evaluate the effects that current stellar modeling uncertainties have on s-process yields. In the present work, we focus on some key physical processes (such as rotation, convection, and mass loss) and on the efficiency of some nuclear processes.

Due to the large number of models included in the FRUITY database, we compute a reduced number of ($M$, $Z$) combinations by analyzing one at a time each of the above-mentioned physical processes, and we derive corrective factors to be applied to models with similar masses ($M$) and metallicities ($Z$). Such a procedure does not introduce biases in our conclusions because we focus our attention on those ($M$, $Z$) combinations where, according to our previous experience, major effects are expected.

### 5.1. Rotation

FRUITY AGB stellar models are representative of the intrinsic carbon stars observed in the disk and in the halo of the Milky Way. However, a comparison between our theoretical curves and spectroscopic data shows that, at fixed metallicity, our models do not cover the observed spread in the s-process indexes. Piersanti et al. (2013) recently demonstrated that a variation in the initial zero-age main sequence (ZAMS) rotational velocity ($v^{rot}_{ZAMS}$) determines a consistent spread in the final surface s-process enhancements and spectroscopic indexes in stars with the same initial mass and metallicity. Rotation-induced instabilities (in particular the Goldreich–Schubert–Fricke instability and meridional circulations) modify the mass extension of both the $^{13}$C and the $^{14}$N pockets and their relative overlap. This is shown in Figure 5, where we report the $^{13}$C and $^{14}$N mass fractions in the upper layers of the He intershell after the fourth TDU episode of a $2\,M_{\odot}$ model with $Z = 10^{-2}$ ([Fe/H] = −0.15) and $v^{rot}_{ZAMS} = 30\,km\,s^{-1}$. We plot chemical profiles at the end of the formation of the $^{13}$C pocket (dotted lines) and at the beginning of the neutron release by the $^{13}$C($\alpha$,n)$^{16}$O reaction (solid lines). The abundance of $^{89}$Y is also plotted to indicate the start of neutron capture processes. With respect to a nonrotating model, the average neutron-to-seed ratio decreases and the production of s-process elements is lower (see also Figure 3 in Piersanti et al. 2013). This is a consequence of the higher abundance of $^{14}$N, a very strong neutron poison, in the $^{13}$C pocket. This also implies that light s elements are less depleted than the heavier ones. It is worth mentioning that the inclusion of rotation does not substantially affect the efficiency of TDU, as evidenced by the almost unaltered surface [C/Fe] (see Piersanti et al. 2013 or the FRUITY database).

**Table 1**
Absolute Percentage Isotopic Abundances with Respect to the Solar Distribution

| Isot. | $\delta_{\odot}$(%) | Reference | No IMS | Rotation | Tail | Reimers | Mloss AGB | Nuclear | SFR+10 |
|---|---|---|---|---|---|---|---|---|---|
| $^{70}$Ge | 16 | 17 | 13 | 17 | 24 | 17 | 17 | 15 | 20 |
| $^{76}$Se | 7 | 20 | 16 | 19 | 30 | 20 | 21 | 18 | 24 |
| $^{80}$Kr | 20 | 20 | 16 | 21 | 32 | 20 | 20 | 18 | 25 |
| $^{82}$Kr | 20 | 26 | 22 | 25 | 42 | 27 | 29 | 26 | 32 |
| $^{86}$Sr | 7 | 52 | 49 | 47 | 90 | 53 | 59 | 52 | 65 |
| $^{87}$Sr | 7 | 51 | 46 | 45 | 84 | 52 | 58 | 52 | 63 |
| $^{96}$Mo | 16 | 110 | 104 | 68 | 135 | 113 | 131 | 104 | 126 |
| $^{100}$Ru | 6 | 124 | 118 | 75 | 151 | 128 | 148 | 123 | 143 |
| $^{104}$Pd | 11 | 130 | 124 | 78 | 157 | 134 | 155 | 129 | 148 |
| $^{110}$Cd | 7 | 123 | 117 | 72 | 144 | 126 | 146 | 122 | 140 |
| $^{116}$Sn | 16 | 112 | 107 | 65 | 130 | 115 | 133 | 109 | 127 |
| $^{122}$Te | 7 | 126 | 120 | 70 | 146 | 130 | 150 | 117 | 140 |
| $^{123}$Te | 7 | 126 | 120 | 71 | 149 | 131 | 149 | 116 | 141 |
| $^{124}$Te | 7 | 135 | 129 | 74 | 155 | 140 | 161 | 124 | 150 |
| $^{128}$Xe | 20 | 158 | 152 | 86 | 181 | 165 | 190 | 152 | 177 |
| $^{130}$Xe | 20 | 154 | 147 | 82 | 175 | 160 | 184 | 148 | 168 |
| $^{134}$Ba | 18 | 216 | 208 | 115 | 257 | 230 | 255 | 193 | 236 |
| $^{136}$Ba | 18 | 192 | 185 | 99 | 217 | 202 | 230 | 188 | 207 |
| $^{142}$Nd | 5 | 170 | 163 | 80 | 210 | 184 | 195 | 174 | 170 |
| $^{148}$Sm | 5 | 159 | 152 | 75 | 202 | 173 | 179 | 152 | 158 |
| $^{150}$Sm | 5 | 148 | 140 | 68 | 175 | 159 | 170 | 145 | 141 |
| $^{154}$Gd | 14 | 103 | 97 | 49 | 115 | 110 | 117 | 127 | 102 |
| $^{160}$Dy | 15 | 139 | 132 | 65 | 173 | 151 | 159 | 134 | 138 |
| $^{170}$Yb | 5 | 154 | 147 | 72 | 201 | 167 | 175 | 150 | 152 |
| $^{176}$Lu | 5 | 183 | 176 | 83 | 224 | 186 | 210 | 189 | 177 |
| $^{176}$Hf | 5 | 175 | 174 | 81 | 225 | 213 | 199 | 179 | 172 |
| $^{186}$Os | 8 | 172 | 164 | 81 | 228 | 189 | 192 | 170 | 168 |
| $^{192}$Pt | 8 | 128 | 120 | 62 | 176 | 140 | 141 | 124 | 126 |
| $^{198}$Hg | 20 | 119 | 112 | 55 | 149 | 128 | 134 | 124 | 116 |
| $^{204}$Pb | 7 | 137 | 130 | 64 | 160 | 148 | 152 | 142 | 133 |

**Note.** Solar percentage errors (taken from Lodders et al. 2009) are also reported (column 2).

Rotational velocities of main sequence stars of spectral classes *A* and *F* span quite a large range, and they can be as high as 300 km s$^{-1}$. On the other hand, asteroseismology measurements seem to indicate that the cores of red giant stars rotate quite slowly (see, e.g., Mosser et al. 2012). This discrepancy is normally attributed to a particularly efficient transfer of angular momentum from the inner zones to the convective envelope or to magnetic braking. In our models we do not account for such an effect, but to compensate for it we use low ZAMS rotation velocities. Thus, we assume $v^{rot}_{ZAMS}$ = 10 km s$^{-1}$ for models with $M \leqslant 2.0\,M_{\odot}$and a slightly larger value for models with $2.0 < M/M_{\odot} \leqslant 4.0$ ($v^{rot}_{ZAMS}$ = 30 km s$^{-1}$). Because of the marginal contribution to the bulk of the s process from IMSs (see Section 4), we do not apply rotating corrective factors to the yields of more massive AGBs (5–6 $M_{\odot}$). In Figure 6 we compare our *Reference* case with a GCE calculation based on stellar models including the effects of rotation (hereinafter the *Rotation* case). The corresponding data are reported in Table 1. As expected, we find a general decrease of the absolute s-process abundances, with the depletion factors increasing for larger atomic masses. With the exception of $^{138}$Ba, s-only nuclei show absolute subsolar percentages. The lightest s-only isotopes (up to $^{86}$Sr) are less depleted than the heavier ones. In fact, the reduced neutron exposure (due to the partial overlap between the $^{13}$C and $^{14}$N pockets) leads to the synthesis of isotopes closer to the iron seeds ($^{56}$Fe), to the detriment of the heavier ones. This is even more evident when looking at the relative overproduction

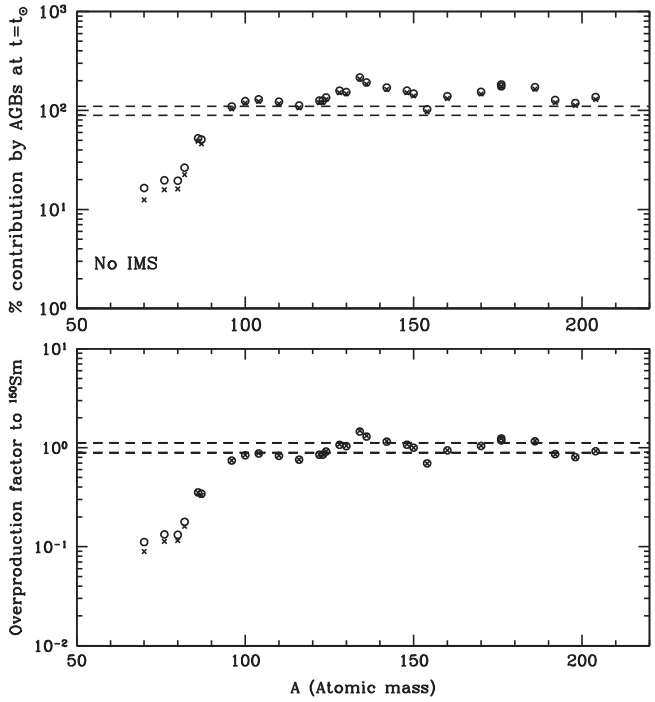



**Figure 4.** As in Figure 3, but including a GCE calculation without the contribution from IMS AGBs (crosses). The *Reference* case (open dots) is shown by comparison. We have omitted error bars for clarity.

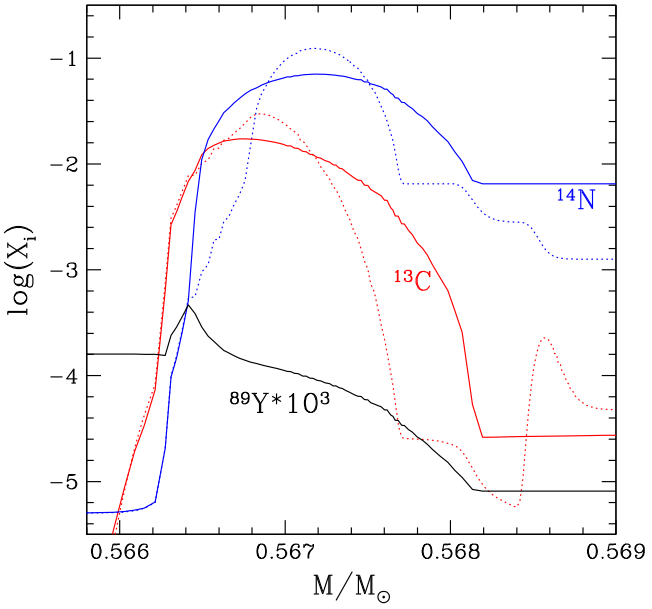



**Figure 5.** $^{13}$C and $^{14}$N profiles after the fourth TDU in a 2 $M_{\odot}$ rotating model with $Z = 10^{-2}$ ([Fe/H] = −0.15) and $v^{rot}_{ZAMS} = 30$ km s$^{-1}$ (solid curves). The $^{89}$Y profile (multiplied by a factor of 1,000) is also displayed. We show $^{13}$C and $^{14}$N profiles at the end of the formation of the $^{13}$C pocket (dotted curves) and when neutrons start being released (solid curves).

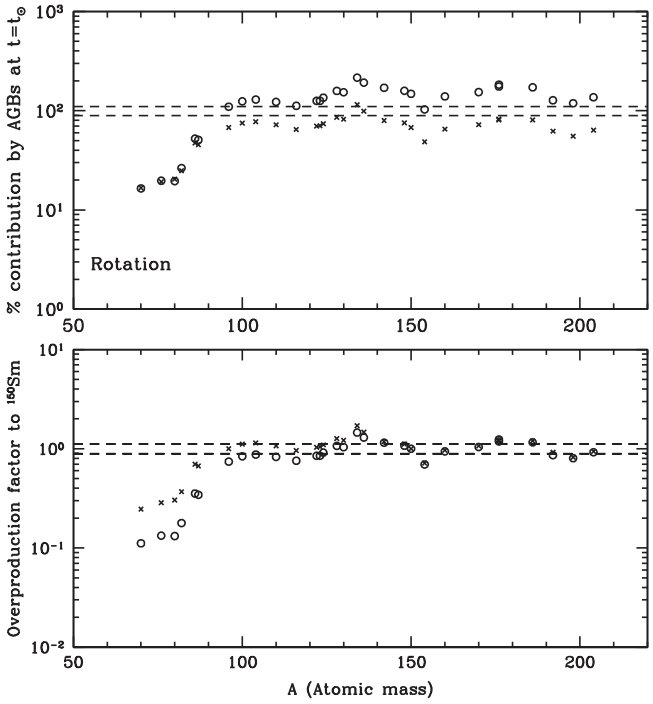



**Figure 6.** As in Figure 4, but including a GCE model with rotating AGB models (crosses).

factors (lower panel of Figure 6). On a relative scale, light s-only isotopes gain more than a factor of two with respect to the *Reference* case, while those in the atomic mass range $96 \leqslant A \leqslant 124$ are now within (or even above) the tolerance region.

Obviously, a different choice of the initial rotational velocities would lead to a different s-only distribution in both the absolute and relative scales. Thus, in principle, a better fit could be found. However, because of the other uncertainty sources affecting stellar models, in particular those related to the treatment of rotation in 1D evolutionary codes (see Piersanti et al. 2013 and references therein), we prefer to highlight general effects related to a physical input (such as rotation) rather than provide a detailed specific recipe to obtain the desired fit.

### 5.2. Convection

In our models, according to the prescriptions of the mixing length theory (MLT; Cox 1968), convective velocities are proportional to the difference between the radiative and the adiabatic temperature gradients. Thus, in the presence of a smooth adiabatic temperature gradient profile, the convective velocity is zero at radiative/convective interfaces. However, when the H-rich envelope penetrates into the He-rich region, which is characterized by a lower opacity, a nonzero convective velocity is found at the inner border of the convective envelope.[8] This is the standard picture of a TDU episode. As a consequence of this abrupt change in the opacity, the radiative/convective interface becomes unstable (see Straniero et al. 2006 for details). However, the steep pressure gradient should limit the penetration of such an instability, and thus the average convective velocity should rapidly drop to zero. We mimic this behavior by assuming that convective velocities follow an exponential decay law below the convective envelope. This has two major consequences: the TDU episode is deeper and, later, a $^{13}$C pocket develops (see Cristallo et al. 2009 for a detailed discussion and for a comparison with techniques used by other groups to handle the formation of the $^{13}$C pocket).

In our FRUITY models, the penetration of protons is inhibited below 2 $H_P$ by the formal Schwarzschild boundary (hereinafter SB). In order to explore the sensitivity of stellar yield and, hence, of GCE calculations on such an assumption, we computed the same FRUITY nonrotating 2 $M_{\odot}$ $Z = 10^{-2}$ ([Fe/H] = −0.15) model, but allowing partial mixing below the SB down to the layer where the convective velocity is $10^{-11}$ times the value at the SB[9](hereinafter the *Tail* case). In the upper panel of Figure 7 we plot the $^{13}$C and $^{14}$N abundances after the third TDU episode of the FRUITY model (solid curves) and the *Tail* model (dotted curves). As can be easily derived, the integrated $^{14}$N mixed below the SB is almost the same for the two cases ($7.6 \times 10^{-5}$ $M_{\odot}$ versus $7.8 \times 10^{-5}$ $M_{\odot}$ for the FRUITY and *Tail* models, respectively), whereas the integrated $^{13}$C is 50% larger in the *Tail* model than in the FRUITY one ($2.3 \times 10^{-5}$ $M_{\odot}$ versus $3.4 \times 10^{-5}$ $M_{\odot}$). This means that the effective $^{13}$C (i.e., the $^{13}$C that effectively contributes to the s process; Cristallo et al. 2011) is nearly twice in the *Tail* model (from $9.2 \times 10^{-6}$ $M_{\odot}$ to $1.8 \times 10^{-5}$ $M_{\odot}$). As a consequence, the overall s-process production increases, as evidenced by the curve in the lower panel of Figure 7, where we plot the differences in the final surface enhancements between the *Tail* and the FRUITY models. The corresponding data are reported in Table 1. As expected, light elements ($Z < 28$) are not affected by the changes in the $^{13}$C tail profile, whereas the three s-process peaks show larger surface enrichments (about +30% for ls and hs and +60% for lead).

[8] We remind readers that the radiative gradient is proportional to the opacity.

[9] This roughly corresponds to (2.2–2.4) $H_P$.

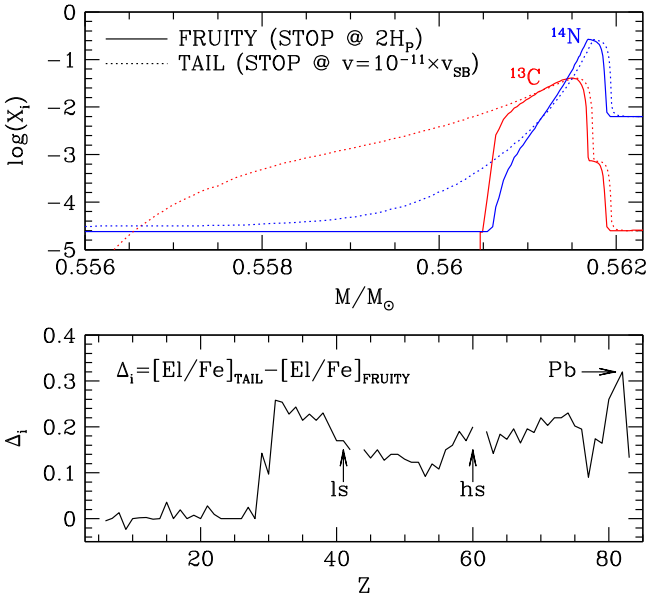



**Figure 7.** Upper panel: $^{13}$C and $^{14}$N profiles after the third TDU of the 2 $M_{\odot}$, $Z = 10^{-2}$ ([Fe/H] = –0.15) models with different prescriptions for the radiative/convective interface treatment. Lower panel: elemental surface differences between the two cases shown in the upper panel.

This additional contribution comes from the portion of the extended $^{13}$C pocket characterized by $5 \times 10^{-3} < X(^{13}\mathrm{C}) < 1 \times 10^{-2}$ (see Figure 7). In our previous models, such a contribution is suppressed because it lies in correspondence to the drop of the $^{13}$C profile. Interestingly, elements normally associated with the weak component (Ge-Ga) are strongly enhanced with respect to the FRUITY model (up to 60%). This is due to the contribution from the inner tail of the $^{13}$C pocket, where neutron densities are lower and, thus, less massive isotopes are synthesized (see, e.g., the $^{69}$Ga profile in Figure 8). In the *Tail* model, neutron-rich isotopes (such as $^{96}$Zr), normally bypassed by the s-process main path, are not enhanced but even mildly depleted with respect to the FRUITY model. This is a consequence of the larger mass extension of the $^{13}$C pocket of the *Tail* case. During the $^{13}$C radiative burning, in fact, neutron-rich isotopes are destroyed more than produced (see, e.g., the $^{96}$Zr profile in Figure 8).

In the upper panel of Figure 9, we show GCE absolute percentage s-only abundances obtained by using AGB models with the new prescription for the lower boundary of the $^{13}$C pocket (*Tail* case). For s-only isotopes with $A \geqslant 96$, we find an increase of s-process absolute percentages (on average +30%), with similar enhancements for light and heavy s-only isotopes (as evidenced by the similar relative distributions reported in the lower panel). Lighter s-only isotopes ($A \leqslant 87$) are more enhanced with respect to the heavier ones because of the contribution from the inner tail of the $^{13}$C pocket. In summary, we find that larger $^{13}$C pockets do not strongly modify the shape of the s-only distribution but do sizeably affect their absolute values (see also Figure 4 in Bisterzo et al. 2014). We also find that the *Tail* case is able to nearly reproduce the entire galactic production of $^{86}$Sr and $^{87}$Sr, in agreement with previous findings (Trippella et al. 2014). However, when compared to other s-only nuclei, Sr s-only isotopes are underproduced, so in our GCE model a certain contribution from the weak s process is still needed.

Note that a rigid shift (in both directions) could also be obtained by assuming a different $\alpha$ parameter of the MLT. Such a parameter is calibrated by reproducing the solar properties with a Standard Solar Model (see Piersanti et al. 2007 for details). However, there is no specific reason to adopt the same $\alpha$ for all of the stellar evolutionary phases (see the discussion in Straniero et al. 2014). Cristallo et al. (2009) already showed that a reduction of the MLT parameter in AGB stars leads to a decrease of the s-process yields. Because this variation does not depend on the metallicity, we expect a corresponding rigid shift in the output of a GCE.

### 5.3. Mass Loss

The poor theoretical knowledge of the stellar mass loss history represents one of the main uncertainties in the computation of AGB stellar models. Low- and intermediate-mass stars lose the majority of their mass during the red giant branch (RGB) and the AGB phases. In 1D stellar evolutionary codes, the mass-loss rate during the RGB phase is commonly parameterized according to the formulation proposed by Reimers (1975):

$$\dot{M} = 4 \times 10^{-13} \frac{L}{gR} \qquad (2)$$

where $\dot{M}$ is in units of $M_{\odot}$ yr$^{-1}$ and other quantities are in solar units. The uncertainty affecting this formula was originally quoted by Reimers to be at least a factor of two either way. Later, Fusi-Pecci & Renzini (1976) introduced a normalization constant in order to reproduce the horizontal branch morphology of globular clusters ($\eta_R = 0.4$).[10] Depending on the mass lost during the RGB phase (and thus on the value of $\eta_R$), stars attain the AGB phase with different envelope masses. Thus, in principle, the RGB mass loss could have an effect on the subsequent AGB nucleosynthesis. Those effects are expected to be important for low-mass stars ($M < 1.5\,M_{\odot}$) because they spend more time in the RGB phase than do larger masses. Moreover, their envelopes are thinner than in more massive stars, so even a small amount of material lost (e.g., 0.1 $M_{\odot}$) can produce sizeable effects on the occurrence of TDU in the subsequent AGB phase (see, e.g., Straniero 2003). To properly determine the effects of RGB mass-loss rate on AGB nucleosynthesis (and thus on the solar s-only distribution), we calculate a set of $M = 1.3\,M_{\odot}$ models at different metallicities with $\eta_R = 0.2$. In Figure 10 we report the variations of the surface abundances ($\Delta_i$) with respect to the corresponding FRUITY cases. We find that $\Delta_i$ are larger at low metallicities (in particular for the heaviest s-only isotopes). This is because at large metallicities this mass experiences a few TDU episodes, even using a milder RGB mass-loss rate. Thus, the final surface s-process enhancement is, in any case, low. By comparison, we also report data relative to a $M = 2$ $M_{\odot}$, $Z = 10^{-2}$ ([Fe/H] = –0.15) model. The low variations found in this case confirm that for massive-enough AGB stars a reduced mass-loss rate during the RGB phase has practically no effect. In Figure 11 we report a GCE model computed with $\eta_R = 0.2$ in stars with $M \leqslant 1.3 M_{\odot}$ (hereinafter the *Reimers* case). We find minor variations in the s-only distribution (see also Table 1), with slightly larger enhancements for the heaviest s-only isotopes ($A > 128$). Our results reinforce the evidence that the major contributors to the solar system s-

[10] FRUITY models adopt this value.

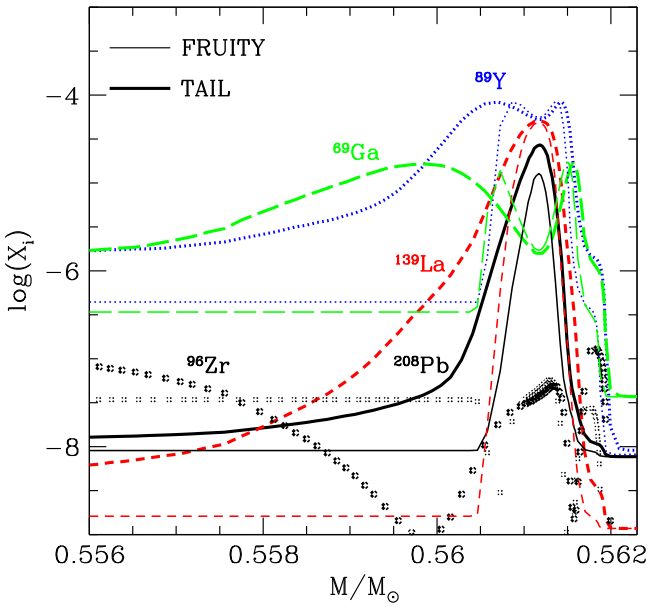



**Figure 8.** Selected key isotope profiles in the $^{13}$C pocket layers after the third TDU of a 2 $M_{\odot}$ and $Z = 10^{-2}$ ([Fe/H] = −0.15) model. Thick and thin curves refer to the *Tail* and FRUITY cases, respectively.

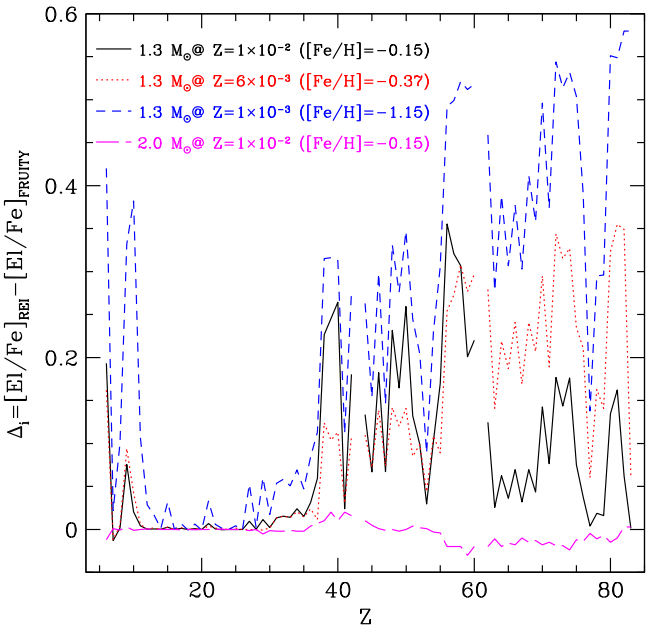



**Figure 10.** Differences in the surface chemical distributions of 1.3 $M_{\odot}$ stars at various metallicities computed with a different RGB mass-loss rate (REI: $\eta_R = 0.2$) with respect to the corresponding FRUITY models (FRUITY: $\eta_R = 0.4$). A 2.0 $M_{\odot}$ star is also reported for comparison.

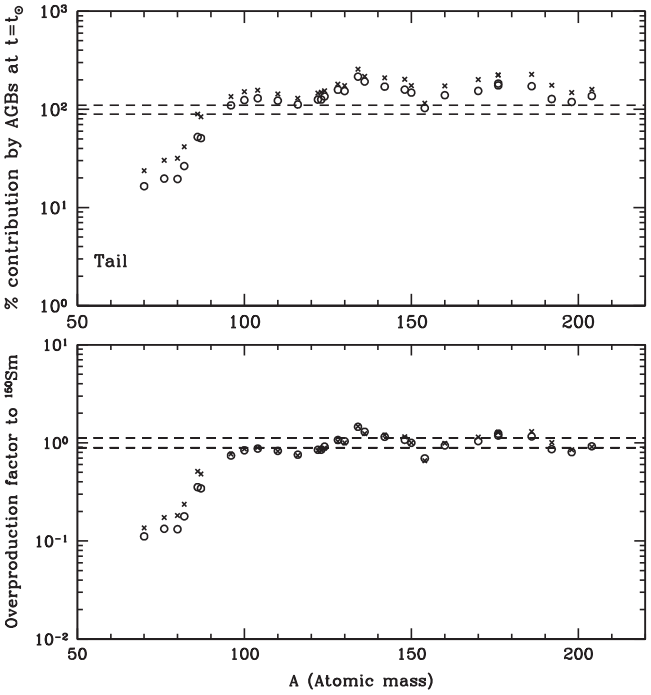



**Figure 9.** As in Figure 4, but including a GCE model based on AGB models handling in a different way the radiative/convective interface at the base of the convective envelope (crosses). See text for details.

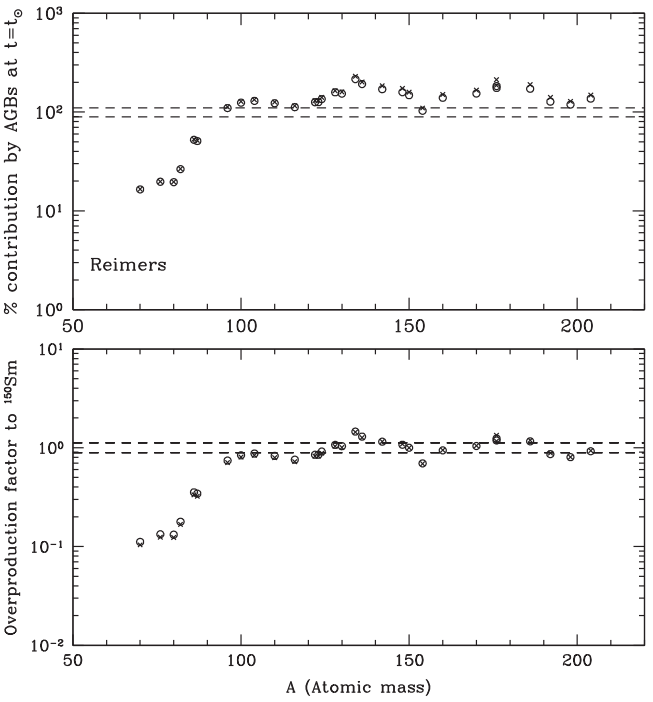



**Figure 11.** As in Figure 4, but including a GCE model with a different RGB mass-loss rate in low-mass stars (crosses).

process inventory are AGB stars in the mass range (1.5–3.0) $M_{\odot}$, as already inferred in Section 3. Their nucleosynthesis is strongly affected by the rate at which they lose mass during the AGB. A viable method to estimate AGB mass loss is based on the observed correlation with the pulsation period (Vassiliadis & Wood 1993). Because the evolution of the pulsation period depends on the variations of radius, luminosity, and mass, this relation provides a simple method to estimate the evolution of the mass-loss rate from basic stellar parameters. In our models, the AGB mass loss is determined according to a procedure similar to the one adopted by Vassiliadis & Wood (1993), but revising the mass loss–period and the period–luminosity relations, taking into account more recent infrared observations of solar-metallicity AGB stars (see Straniero et al. 2006 and references therein). It has been demonstrated that AGB mass-loss rates are mildly dependent on the metallicity (Groenewegen et al. 2007; Lagadec et al. 2008), and thus we applied the

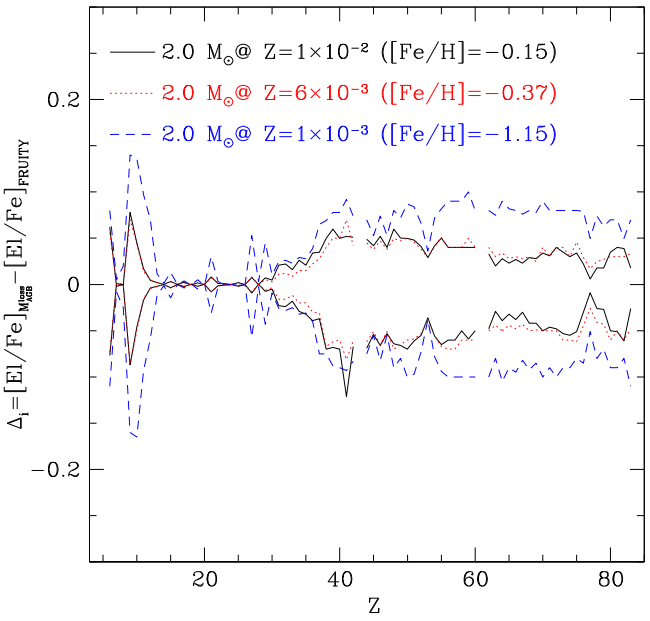



**Figure 12.** Differences with respect to FRUITY models in the final surface chemical distributions of 2.0 $M_{\odot}$ stars at various metallicities computed with an increased or decreased AGB mass-loss rate. Our standard AGB mass-loss rate has been described in Straniero et al. (2006). Negative differences are obtained with an increased mass-loss rate (similarly, positive differences are found for models with a reduced AGB mass-loss rate). As expected, elements whose AGB production is negligible show null differences (i.e., they have the same final surface abundances of the corresponding FRUITY models).

same period–mass loss relation for all AGB models present in the FRUITY database. Nevertheless, it is worth noting that, when a fixed period is defined, the observational data show quite a large scatter. In a period–mass loss plot, a theoretical curve constructed when reducing by a factor of two the mass-loss rate at a fixed period still lies within the observed spread (see Figure 8.10 of Cristallo 2006). This still holds for a mass-loss rate increased by a factor of two. In order to quantify the effects on the s-only distribution induced by a variation of the AGB mass-loss rate, we compute some AGB models with a milder and stronger period–mass loss relations. In Figure 12 we show the results on the final surface distributions of 2 $M_{\odot}$ stellar models at various metallicities. In the plot, $\Delta_i$ represents the difference between models computed with the standard $\dot{M}$–period relation (Straniero et al. 2006) and the modified ones. Obviously, positive differences are obtained with a milder mass-loss rate, while negative differences with the stronger one. Heavy-element surface variations are below 0.1 dex (25%) for the whole s-process distribution, being slightly larger at low metallicity. Thus, we expect that a modified $\dot{M}$–period relation in the AGB phase will produce an almost rigid shift (upward or downward, depending on the adopted mass-loss law) of the s-process isotopes. In order to verify this statement, we compute a GCE model with a milder $\dot{M}$–period relation during the AGB phase (hereinafter the *Mloss AGB* case). The results are shown in Figure 13; the corresponding data are reported in Table 1. As expected, for s-only isotopes with $A \geqslant 96$, there is an almost rigid upper shift of solar percentages (~25%). In summary, a rigid shift (upward or downward) of the s-process isotopic inventory can be obtained by adopting a different prescription for the AGB mass-loss rate within the intrinsic observed scatter in the $\dot{M}$–period relation.

### 5.4. Efficiency of Nuclear Processes

In previous sections, we demonstrated that different prescriptions on physical processes can lead to appreciable variations of the s-only inventory. In this section we concentrate on strong and weak nuclear processes. We refer to Cristallo et al. (2011) for a list of the adopted reaction rates in FRUITY models. Here, we focus on the uncertainties affecting the rates of

1. nuclear processes determining the abundances of s-only isotopes close to s-process branchings;
2. neutron sources in AGB stars, i.e., the $^{13}C(\alpha,n)^{16}O$ and $^{22}Ne(\alpha,n)^{25}Mg$ reactions;
3. the major neutron poison in AGB stars, i.e., the $^{14}N(n,p)^{14}C$ reaction.

By means of the first test we can quantify local variations of s-only isotopes, and the others allow us to determine if nuclear processes are able to shape the whole s-only distribution.

#### 5.4.1. S-process Branchings

We focus on the branchings at $^{134}Cs$ and at $^{154}Eu$, which determine the surface abundances of $^{134}Ba$ and $^{154}Gd$ (over-produced and underproduced with respect to $^{150}Sm$ in our GCE models, respectively). In Figure 14 we report the main s-process path in the regions of the nuclide chart corresponding to the two s-process branching points. The unstable isobars have $\beta$ decay timescales of the order of years (2.1 and 8.8 yr in laboratory conditions for $^{134}Cs$ and $^{154}Eu$, respectively). Thus, their decays are faster than the corresponding neutron captures during radiative $^{13}C$ burning, but long enough to allow the opening of s-process branchings during the convective $^{22}Ne(\alpha,n)^{25}Mg$ burning. Direct measurements of the $^{134}Cs(n,\gamma)^{135}Cs$ reaction are prohibitive (Patronis et al. 2004), and for the neutron capture on $^{154}Eu$ only a dated activation measurement is available (Anderl et al. 1981). We explore the effects of varying their neutron cross sections by adopting the uncertainties recently provided by Rauscher (2012) ( $\pm$10% and $\pm$50% for $^{134}Ba$ and $^{154}Gd$, respectively). The $\beta$ decay rates are taken from Takahashi & Yokoi (1987), and corresponding uncertainties (a factor of three) are taken from Goriely (1999).

In Figure 15 we report the differences (filled dark circles) in the yields of a 2 $M_{\odot}$ $Z = 10^{-2}$ ([Fe/H] = −0.15) model with respect to a FRUITY model by modifying neutron cross sections and $\beta$ decays in the following way:

1. upper limit for the $^{134}Cs$ neutron capture cross section;
2. lower limit for the $\beta^-$ decay rate of $^{134}Cs$ into $^{134}Ba$;
3. lower limit for the $^{154}Eu$ neutron capture cross section;
4. upper limit for the $\beta^-$ decay rate of $^{154}Eu$ into $^{154}Gd$.

These choices aim at minimizing the $^{134}Ba$ production and at maximizing the $^{154}Gd$ production. The plotted quantities are normalized to variations in $^{150}Sm$ yields (thus, unity means no variation with respect to $^{150}Sm$). We find a 5% reduction of $^{134}Ba$ yield and a 30% increase of $^{154}Gd$ yield. Note that these numbers refer to 2 $M_{\odot}$ models: for more massive AGB stars (e.g., 3.0–4.0 $M_{\odot}$), these effects are larger.

#### 5.4.2. S-process Neutron Sources

Then, we verify if the solar s-only distribution is modified when adopting recently published rates for the two major neutron sources in AGB stars, i.e., the $^{13}C(\alpha,n)^{16}O$ and the

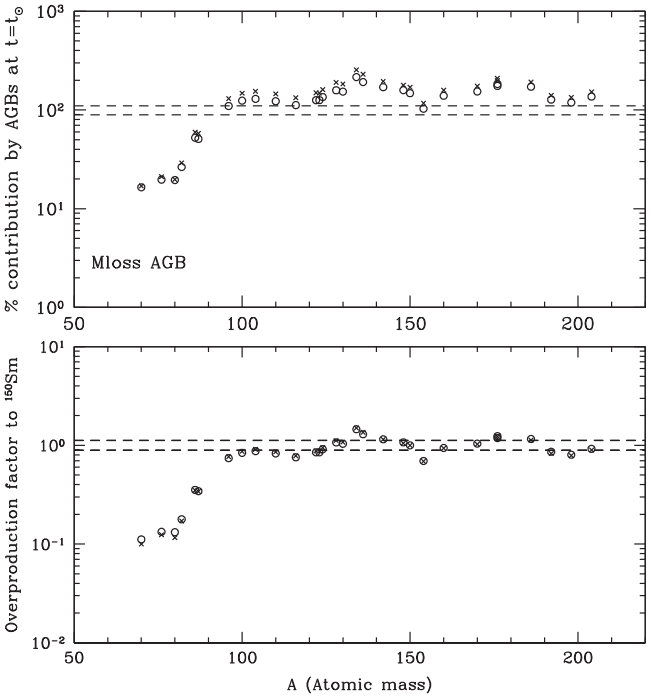



**Figure 13.** As in Figure 4, but including a GCE model obtained by assuming a lower AGB mass-loss rate (crosses). See text for details.

$^{22}$Ne($\alpha$,n)$^{25}$Mg reactions. Whereas the first reaction releases neutrons in radiative conditions during interpulse periods, the latter burns in a convective environment during TPs. For the $^{13}$C($\alpha$,n)$^{16}$O reaction we used the value proposed by La Cognata et al. (2013), and for the $^{22}$Ne($\alpha$,n)$^{25}$Mg reaction the value suggested by Longland et al. (2012) is adopted. With respect to our reference rates (Drotleff et al. 1993 and Kaeppeler et al. 1994, respectively), both of them are about 20% higher at the temperatures of interest. The combined effect induced by the new $^{13}$C($\alpha$,n)$^{16}$O and $^{22}$Ne($\alpha$,n)$^{25}$Mg reactions is an overall slight increase of the whole s-only distribution. This derives from the fact that with a higher $^{13}$C($\alpha$,n)$^{16}$O reaction rate the $^{13}$C fully burns in radiative conditions, whereas when using the reference rate some of the $^{13}$C in the first pockets can be engulfed in the convective shells generated by TPs (Cristallo et al. 2009). In that case, only neutron-rich isotopes such as $^{60}$Fe and $^{96}$Zr are synthesized. This is confirmed by the strongly reduced $^{96}$Zr abundance (open pentagon) we obtain in this model,[11] despite the increased $^{22}$Ne($\alpha$,n)$^{25}$Mg reaction rate. On a relative scale, we notice a marginal decrease of the lighter s-only isotopes with respect to the heavy ones (triangles in Figure 15). The increase of the $^{22}$Ne($\alpha$,n)$^{25}$Mg reaction does not produce sizeable effects on the $^{134}$Ba production (see also Liu et al. 2014), which is at the same level of s-only isotopes with $96 \leqslant A \leqslant 130$. Such a result further confirms that this reaction is only marginally activated in low-mass AGB stars.

### 5.4.3. S-process Poisons

Major neutron poisons in AGB stars are the $^{14}$N(n,p)$^{14}$C and the $^{26}$Al(n,p)$^{26}$Mg reactions, working in $^{13}$C pockets and during TPs, respectively. In consideration of the weak activation of the $^{22}$Ne($\alpha$,n)$^{25}$Mg neutron source, we concentrate on the first reaction only. Our reference rate is taken from Koehler & O'brien (1989). In Figure 15 we report the variations in s-only isotope yields (squares) by considering an increased rate of 10%. We find a general decrease of heavy s-only isotopes, which translates into a general overproduction of light s-only isotopes with respect to $^{150}$Sm (+8% on average). This is because an increased poison effect reduces the s-process efficiency and, thus, its capability to bypass the bottleneck at $Z = 50$. Similar results (but in the opposite direction) are expected when considering the lower limit of the $^{14}$N(n,p)$^{14}$C reaction. Note that this effect is less relevant for higher masses (in which the $^{22}$Ne($\alpha$,n)$^{25}$Mg is more efficiently activated), and it practically vanishes at low metallicities (where the $Z = 50$ bottleneck is more easily bypassed because of the larger neutron-to-seed ratio).

[11] A similar decrease is also found for $^{60}$Fe.

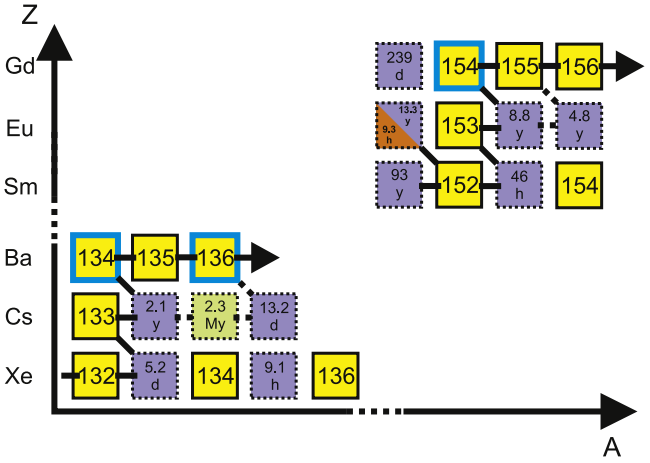



**Figure 14.** s-process main path in the region of $^{134}$Cs and $^{154}$Eu branching points.

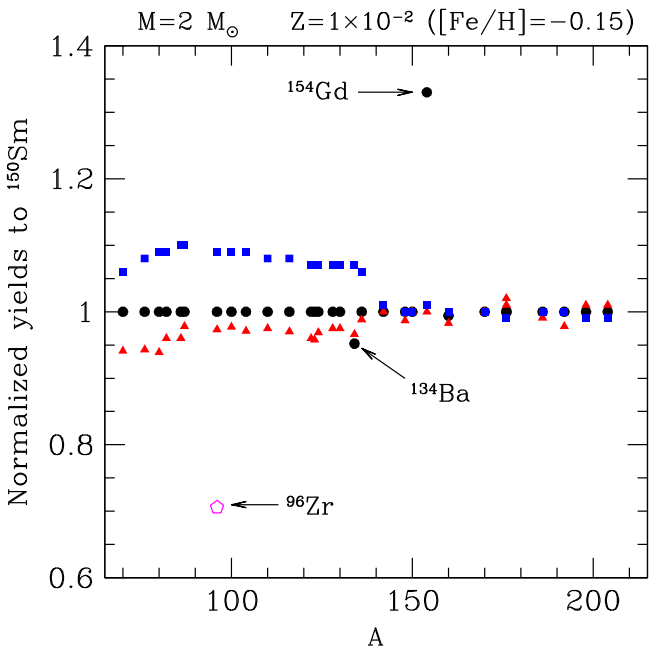



**Figure 15.** Differences in the yields of a $2\,M_\odot$ model with $Z = 10^{-2}$ ([Fe/H] = −0.15) obtained by varying strong and weak reaction rates (dots: variations of nuclear process efficiencies in correspondence to $^{134}$Cs and $^{154}$Eu branching; triangles: variations of neutron source cross sections; squares: variations of neutron poison cross sections). Differences are normalized to variations in $^{150}$Sm yields. See text for details.

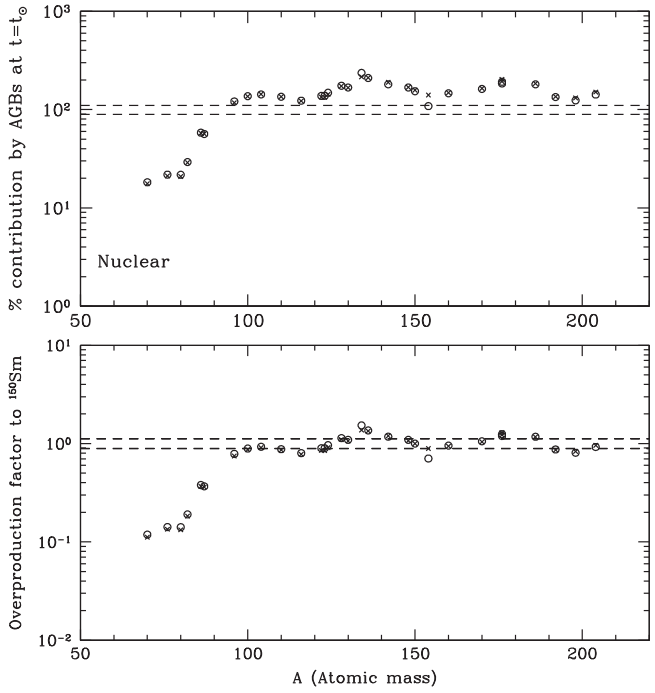



**Figure 16.** As in Figure 4, but including a GCE model with different prescriptions on selected strong and weak nuclear processes (crosses). See text for details.

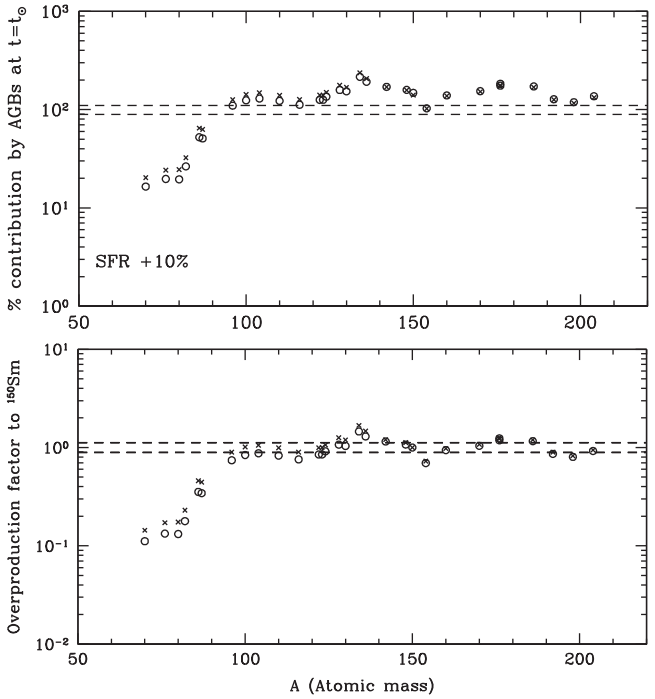



**Figure 17.** As in Figure 4, but including a GCE model with an increased SFR of +10% (crosses). See text for details.

#### 5.4.4. Effects on a GCE Model

In Figure 16 we report the results of a GCE model in which we take into account all of the previously described modified rates (hereinafter the *Nuclear* case). The corresponding data are reported in Table 1. Variations in the cross sections of neutron sources and of the major neutron poison in AGB stars do not lead to significative changes in the global s-only isotope distribution. However, this is not the case for the solar abundances of s-only isotopes close to s-process branchings. In fact, we find that the solar $^{134}$Ba and $^{154}$Gd percentages decrease and increase by more than 20%, respectively. However, we remark that the uncertainties in the $\beta$ decay rates (which mainly determine the differences shown in Figures 15 and 16) are rough estimates and, thus, larger isotopic variations cannot be a priori excluded. A further theoretical nuclear analysis on this topic would be highly desirable.

## 6. GALACTIC CHEMICAL EVOLUTION MODEL UNCERTAINTIES

It is important to remember that GCE models also strongly depend on the adopted inputs, such as the SFR, the IMF, or the type Ia supernovae evolutionary scenario (see Section 4). In fact, each of these items influences the amount of metals locked in or released by stars at different epochs. The relevance of their impact would depend on how much their variations (within the current uncertainties) would affect the derived age–metallicity relation. For instance, a faster increase of the ISM metallicity would imply a lower contribution from metal-poor stars because there would be less time to form them. Thus, the contribution from metal-rich AGB stars to the solar system s-process distribution would be larger, and, consequently, the production of s-only isotopes with $96 \leqslant A \leqslant 124$ would be increased (Maiorca et al. 2012; see also Trippella et al. 2014). In fact, the higher the iron seeds number the lower the atomic mass of the synthesized s-process nuclei. We plan to systematically study the impact of different choices of the GCE input parameters on the s-only distribution in a forthcoming paper. Here we only show the effects that a variation of the SFR has on the solar s-only isotopic distribution.

Observations of various SFR indicators in galaxies reveal that star formation occurs in different ways, depending on the galaxy type. There is no theory to predict star formation on large scales in a galaxy given the many physical ingredients that may affect the SFR. In Figure 2 we show the age–metallicity relation obtained by assuming an increased SFR at all epochs (+10%; dashed curve) with respect to our *Reference* case. The corresponding data are reported in Table 1. We will refer to this case as SFR+10. Actually, we have just changed the $\alpha$ parameter in Schmidt's law by 10% because with this choice it is still possible to account for, within observational uncertainties, all of the solar neighborhood observables mentioned in Section 4. A larger variation of the SFR would imply a new calibration of the GCE model itself, and, therefore, it would be difficult to disentangle the effects related to the change in the SFR from those connected to the new parameter set adopted to again fit observables. As shown in Figure 17, the variation of the SFR has an appreciable effect on the s-only isotope distribution. We notice a slight increase of light s-only isotopes and a more consistent decrease of the heavy ones. As a consequence, on a relative scale, light s-only isotopes with $96 \leqslant A \leqslant 136$ are overproduced with respect to the heavier ones by 18% on average.

## 7. DISCUSSION AND CONCLUSIONS

In this paper we verify if our FUNS stellar yields (available on the FRUITY database), used in a galactic chemical

evolution model, can reproduce the distribution of s-only isotopes characterizing the protosolar nebula. Those nuclei are only synthesized by the s process and, thus, are exceptional markers of the evolution of past galactic AGB populations. At odds with previous studies based on postprocess calculations (Bisterzo et al. 2014; Trippella et al. 2014), we use in our analysis AGB stellar yields obtained by means of stellar evolutionary calculations fully coupled to an extended nuclear network.

In our GCE models, we find that the contribution to the solar system s-only distribution from low-mass AGB stars ($M < 1.5\,M_{\odot}$) and from intermediate-mass AGB stars ($M > 4\,M_{\odot}$) is marginal. Thus, we confirm that the bulk of the s process comes from AGB stars with masses of $(1.5 - 3.0)\,M_{\odot}$. Another major result of this study is that we do not miss any contribution to the solar system s-only distribution in the atomic mass range $96 \leqslant A \leqslant 124$, as claimed by Travaglio et al. (2004) and Bisterzo et al. (2014). Our reference GCE model, in fact, predicts an overall supersolar s-only distribution ($\sim +45\%$ on average). When observational and nuclear errors are taken into account, the distribution relative to $^{150}$Sm can be considered flat, even if a lower production is found for s-only nuclei with $96 \leqslant A \leqslant 124$. We investigate if current uncertainties affecting stellar models can lead to a better fit to the solar system s-only isotopic distribution. The inclusion of rotation in our stellar models implies a general suppression of the s process, with larger depletion factors for the heaviest s-only isotopes. On a relative scale, this implies a larger contribution to light s-only isotopes and, thus, a flatter s-only distribution. Different prescriptions for convection efficiency and for the treatment of the unstable inner border of the convective envelope during TDU episodes produce nearly rigid shifts of the entire s-only distribution. The same result can be achieved by adopting a different mass-loss rate during the AGB phase. Current nuclear uncertainties affecting strong and weak reactions allow for important improvements in the determination of some s-only isotopes (such as $^{134}$Ba and $^{154}$Gd). The need for revised $\beta$ decay rates with respect to those published by Takahashi & Yokoi (1987) is highly compelling.

In the past, the nucleosynthesis of s-only isotopes has been closely related to that of $^{208}$Pb. Although such a nucleus is not a pure s-process isotope, a large percentage of its solar abundance is ascribed to the s process, the estimates varying from about 85% (Cowan et al. 1999) to 98% (Bisterzo et al. 2014). Our reference model slightly overestimates its absolute solar abundance (108%); as a consequence, about 27% of $^{208}$Pb is missing with respect to $^{150}$Sm (which has an absolute percentage solar abundance of 148%). Taking into consideration its still uncertain s-process contribution and the observational error in the determination of its solar abundance, we are missing about 10% of solar $^{208}$Pb at a minimum. Note, however, that at odds with the s-only isotopes studied in this paper, this isotope could receive a nonnegligible contribution from very low metallicity AGB stars (see Figure 1), which are not taken into account in our simplified GCE model. Thus, we can assume our $^{208}$Pb production as a sort of lower limit. Concerning the test models previously discussed, we find that the absolute abundance of $^{208}$Pb roughly scales as the $^{150}$Sm one. On a relative scale, minor variations (<5%) are found in the majority of tests, apart from the *Rotation* case (−9%) and the *Tail* case (+22%). The latter could be a good candidate to compensate for the relative $^{208}$Pb underproduction found in the *Reference* case.

It is important to remark that, in addition to the uncertainties of AGB stellar models discussed here, other uncertainties may affect the predicted s-only distribution. As is well known, AGB stars at various metallicities contribute differently to the three s-process peaks. Thus, if the contribution from stars at large $Z$ is favored (Trippella et al. 2014), a flatter relative s-only distribution may be found. Thus, the hypothesis on the existence of a LEPP process also relies on the uncertainties currently affecting galactic chemical evolution models. We verified that an increase of the SFR at all epochs leads to a faster increase of the ISM metallicity and, thus, to a larger contribution from metal-rich stars. As a consequence, we obtain a larger production of light s-only isotopes with respect to the heavy ones and, consequently, a flatter distribution.

In conclusion, our full stellar evolutionary models coupled to a GCE model for the solar neighborhood do not necessarily require a LEPP mechanism to increase the solar system s-only abundances in the range $96 \leqslant A \leqslant 124$. However, owing to the uncertanties still affecting both stellar and galactic chemical evolution models, we cannot a priori definitely rule out the existence of additional contributions to the solar system s-only isotope distribution. Note that the models presented in this paper cannot certify (or rule out) the existence of a metal-poor primary LEPP, invoked to explain the abundances of a large group of light elements in low-metallicity, r-process enhanced halo stars.

We thank the referee for valuable comments and suggestions that improved the quality of this paper. This work was supported by Italian grants RBFR08549F-002 (FIRB 2008 program), PRIN-MIUR 2012 “Nucleosynthesis in AGB stars: An integrated approach” project (20128PCN59), and from Spanish grants AYA2008-04211-C02-02 and AYA-2011-22460.

## REFERENCES

Abia, C., Canal, R., & Isern, J. 1991, ApJ, 366, 198
Abia, C., Isern, J., & Canal, R. 1995, A&A, 298, 465
Adibekyan, V. Z., Sousa, S. G., Santos, N. C., et al. 2012, A&A, 545, A32
Anderl, R. A., Schmittroth, F., & Harker, Y. D. 1981, Integral-capture Measurements and Cross-section Adjustments for Nd Sm, and Eu
Arlandini, C., Käppeler, F., Wisshak, K., et al. 1999, ApJ, 525, 886
Beer, H., Walter, G., & Kaeppeler, F. 1992, ApJ, 389, 784
Bensby, T., Feltzing, S., & Oey, M. S. 2014, A&A, 562, A71
Bisterzo, S., Travaglio, C., Gallino, R., Wiescher, M., & Käppeler, F. 2014, ApJ, 787, 10
Boissier, S., & Prantzos, N. 1999, MNRAS, 307, 857
Bravo, E., & Martínez-Pinedo, G. 2012, PhRvC, 85, 055805
Busso, M., Gallino, R., & Wasserburg, G. J. 1999, ARA&A, 37, 239
Casagrande, L., Schönrich, R., Asplund, M., et al. 2011, A&A, 530, A138
Chieffi, A., & Limongi, M. 2004, ApJ, 608, 405
Chieffi, A., Limongi, M., & Straniero, O. 1998, ApJ, 502, 737
Chieffi, A., & Straniero, O. 1989, ApJS, 71, 47
Cowan, J. J., Pfeiffer, B., Kratz, K.-L., et al. 1999, ApJ, 521, 194
Cox, J. P. 1968, in Principles of Stellar Structure, Vol. 1 (New York: Gordon & Breach), 1
Cristallo, S. 2006, PASP, 118, 1360
Cristallo, S., Piersanti, L., Straniero, O., et al. 2011, ApJS, 197, 17
Cristallo, S., Straniero, O., Gallino, R., et al. 2009, ApJ, 696, 797
Cristallo, S., Straniero, O., Lederer, M. T., & Aringer, B. 2007, ApJ, 667, 489
Denissenkov, P. A., & Tout, C. A. 2003, MNRAS, 340, 722
Drotleff, H. W., Denker, A., Knee, H., et al. 1993, ApJ, 414, 735
Fusi-Pecci, F., & Renzini, A. 1976, A&A, 46, 447
Gallino, R., Arlandini, C., Busso, M., et al. 1998, ApJ, 497, 388

Goriely, S. 1999, A&A, 342, 881
Goswami, A., & Prantzos, N. 2000, A&A, 359, 191
Greggio, L., & Renzini, A. 1983, A&A, 118, 217
Groenewegen, M. A. T., Wood, P. R., Sloan, G. C., et al. 2007, MNRAS, 376, 313
Herwig, F., Bloecker, T., Schoenberner, D., & el Eid, M. 1997, A&A, 324, L81
Kaeppeler, F., Wiescher, M., Giesen, U., et al. 1994, ApJ, 437, 396
Kappeler, F., Beer, H., & Wisshak, K. 1989, RPPh, 52, 945
Käppeler, F., Gallino, R., Bisterzo, S., & Aoki, W. 2011, RvMP, 83, 157
Kobayashi, C., Tsujimoto, T., & Nomoto, K. 2000, ApJ, 539, 26
Koehler, P. E., & O'brien, H. A. 1989, PhRvC, 39, 1655
Kubryk, M., Prantzos, N., & Athanassoula, E. 2013, MNRAS, 436, 1479
La Cognata, M., Spitaleri, C., Trippella, O., et al. 2013, ApJ, 777, 143
Lagadec, E., Zijlstra, A. A., Matsuura, M., et al. 2008, MNRAS, 383, 399
Li, W., Chornock, R., Leaman, J., et al. 2011, MNRAS, 412, 1473
Liu, N., Gallino, R., Bisterzo, S., et al. 2014, ApJ, 788, 163
Lodders, K., Palme, H., & Gail, H.-P. 2009, LanB, 4, 44
Longland, R., Iliadis, C., & Karakas, A. I. 2012, PhRvC, 85, 065809
Maiorca, E., Magrini, L., Busso, M., et al. 2012, ApJ, 747, 53
Micali, A., Matteucci, F., & Romano, D. 2013, MNRAS, 436, 1648
Montes, F., Beers, T. C., Cowan, J., et al. 2007, ApJ, 671, 1685
Mosser, B., Goupil, M. J., Belkacem, K., et al. 2012, A&A, 548, A10
Nissen, P. E., Chen, Y. Q., Carigi, L., Schuster, W. J., & Zhao, G. 2014, A&AA, 568, A25
Pagel, B. E. J. 2009, Nucleosynthesis and Chemical Evolution of Galaxies (Cambridge: Cambridge Univ. Press)
Patronis, N., Dababneh, S., Assimakopoulos, P. A., et al. 2004, PhRvC, 69, 025803
Piersanti, L., Cristallo, S., & Straniero, O. 2013, ApJ, 774, 98
Piersanti, L., Straniero, O., & Cristallo, S. 2007, A&A, 462, 1051
Pignatari, M., Gallino, R., Heil, M., et al. 2010, ApJ, 710, 1557
Ramírez, I., Allende Prieto, C., & Lambert, D. L. 2013, ApJ, 764, 78
Rauscher, T. 2012, ApJL, 755, L10
Reimers, D. 1975, MSRSL, 8, 369
Roskar, R., Debattista, V. P., Stinson, G. S., et al. 2008, ApJL, 675, L65
Schönrich, R., & Binney, J. 2009, MNRAS, 396, 203
Sneden, C., Cowan, J. J., & Gallino, R. 2008, ARA&A, 46, 241
Straniero, O., Cristallo, S., & Piersanti, L. 2014, ApJ, 785, 77
Straniero, O., Domínguez, I., Imbriani, G., & Piersanti, L. 2003, ApJ, 583, 878
Straniero, O., Gallino, R., Busso, M., et al. 1995, ApJL, 440, L85
Straniero, O., Gallino, R., & Cristallo, S. 2006, NuPhA, 777, 311
Takahashi, K., & Yokoi, K. 1987, ADNDT, 36, 375
Travaglio, C., Galli, D., Gallino, R., et al. 1999, ApJ, 521, 691
Travaglio, C., Gallino, R., Arnone, E., et al. 2004, ApJ, 601, 864
Travaglio, C., Gallino, R., Busso, M., & Gratton, R. 2001, ApJ, 549, 346
Trippella, O., Busso, M., Maiorca, E., Käppeler, F., & Palmerini, S. 2014, ApJ, 787, 41
Vassiliadis, E., & Wood, P. R. 1993, ApJ, 413, 641